Opto-Electronic Advances

ISSN 2096-4579 CN 51-1781/TN

Fast source mask co-optimization method for high-NA EUV lithography

Ziqi Li, Lisong Dong, Xu Ma and Yayi Wei

Citation: Li ZQ, Dong LS, Ma X, et al. Fast source mask co-optimization method for high-NA EUV lithography. *Opto-Electron Adv* **7**, 230235(2024).

https://doi.org/10.29026/oea.2024.230235

Received: 24 December 2023; Accepted: 22 March 2024; Published online: 25 April 2024

Opto-Electronic Advances

Article

April 2024, Vol. 7, No. 4

DOI: 10.29026/oea.2024.230235

Fast source mask co-optimization method for high-NA EUV lithography

Ziqi Li[1,3], Lisong Dong[1,3,4], Xu Ma[2] and Yayi Wei[1,3,4]*

Extreme ultraviolet (EUV) lithography with high numerical aperture (NA) is a future technology to manufacture the integrated circuit in sub-nanometer dimension. Meanwhile, source mask co-optimization (SMO) is an extensively used approach for advanced lithography process beyond 28 nm technology node. This work proposes a novel SMO method to improve the image fidelity of high-NA EUV lithography system. A fast high-NA EUV lithography imaging model is established first, which includes the effects of mask three-dimensional structure and anamorphic magnification. Then, this paper develops an efficient SMO method that combines the gradient-based mask optimization algorithm and the compressive-sensing-based source optimization algorithm. A mask rule check (MRC) process is further proposed to simplify the optimized mask pattern. Results illustrate that the proposed SMO method can significantly reduce the lithography patterning error, and maintain high computational efficiency.

Keywords: computational lithography; high-NA EUV lithography; source-mask co-optimization; lithography imaging model

Li ZQ, Dong LS, Ma X et al. Fast source mask co-optimization method for high-NA EUV lithography. *Opto-Electron Adv* **7**, 230235 (2024).

Introduction

Extreme ultraviolet (EUV) lithography with high numerical aperture (NA) is a future technology to manufacture very tiny layout patterns on the cutting-edge integrated circuits (IC)[1,2]. The resolution R of lithography system is given by the Rayleigh's equation[3,4]: $R = k_1\lambda/NA$, where k_1 is a process-dependent factor, λ is the wavelength of light source, and NA is the numerical aperture of the projection system. Currently, high-NA (NA=0.55) EUV lithography system can be used to fabricate the IC patterns with 7 nm critical dimension (CD) on the wafer. Figure 1 shows the projection systems for the 1.35NA deep ultraviolet (DUV) immersion lithography, 0.33NA EUV lithography, and 0.55NA EUV lithography, respectively[2]. Many unique designs are implanted in the high-NA EUV lithography system, including the reflective mask, reflective optics system, anamorphic projection system and drilled mirror[1,2].

Except for the special designs, the prominent mask three-dimensional (3D) effect in EUV lithography will reduce the image fidelity and cause the patterning shift through focus[5–7]. Specifically, the complicated interaction between EUV electromagnetic waves and mask 3D structures will significantly influence the complex amplitude of the mask diffraction near-field (DNF). Other effects, like aberration and flare, can also impact the

[1]EDA Center, Institute of Microelectronics of Chinese Academy of Sciences, Beijing 100029, China; [2]Key Laboratory of Photoelectronic Imaging Technology and System of Ministry of Education of China, School of Optics and Photonics, Beijing Institute of Technology, Beijing 100081, China; [3]University of Chinese Academy of Sciences, Beijing 100049, China; [4]Guangdong Greater Bay Area Applied Research Institute of Integrated Circuit and Systems, Guangzhou 510700, China.

*Correspondence: YY Wei, E-mail: weiyayi@ime.ac.cn

Received: 24 December 2023; Accepted: 22 March 2024; Published online: 25 April 2024

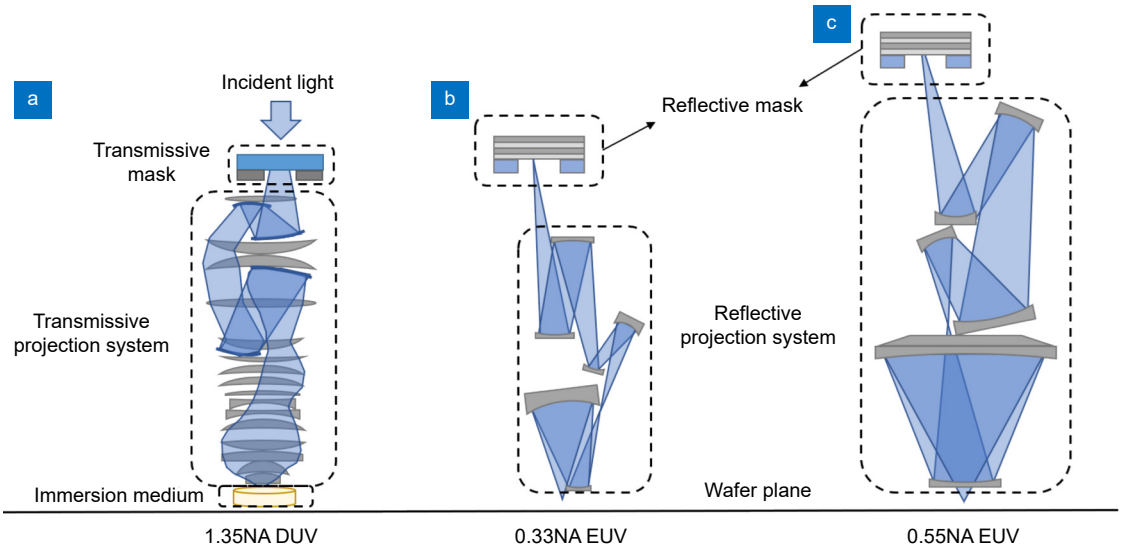

Fig. 1 | Sketches of the projection systems for the (**a**) 1.35NA DUV immersion lithography, (**b**) 0.33NA EUV lithography, and (**c**) 0.55NA EUV lithography.

lithography imaging performance[8], which are beyond the scope of this work.

On the other hand, the source-mask co-optimization (SMO) is an important method to improve the image quality in advanced lithography process beyond 28 nm technology node[3,4]. The concept of SMO was first introduced in 2002[9]. Compared with the optical proximity correction (OPC) technology, SMO optimizes the source and mask jointly, which increases the degrees of optimization freedom. By reducing the factor k_1 in the Rayleigh's equation, SMO can significantly improve the imaging resolution of lithography system, thus further expanding the process window and improving the yield[10,11].

Up to now, most of researches in this field proposed to study the SMO methods for DUV lithography, and several pervious works focused on the SMO methods for EUV lithography. A gradient-based SMO method for 0.33NA EUV lithography was proposed in ref.[12], where the thin-mask model was used to calculate the image, so that the mask 3D effect was ignored. In another study[13], the cost function of SMO included a resist sensitivity penalty term to increase the image contrast and exposure latitude. In ref.[14], an SMO method was developed for the 0.33NA EUV lithography system, where a heuristic algorithm and an analytical thick-mask model were applied to solve the optimization problem. However, most of those works failed to consider the complicated mask 3D effects under the partially coherent illumination condition. In addition, those works were proposed for low-NA (*NA*=0.33) EUV lithography systems, which cannot take into account the characteristics of high-NA EUV lithography systems.

In this work, an SMO method is proposed for the high-NA EUV lithography system. To efficiently simulate the mask 3D effects under partially coherent illumination, a decomposed learning based thick-mask model is implanted in the lithography imaging model. Several convolution filters are pre-calibrated from the DNF database. Given a mask layout, it is firstly decomposed into several local segments according to its geometric features. The local thick-mask DNFs are then calculated by convoluting the segment patterns with the corresponding filter kernels. Finally, all of the local DNF segments are put together to assemble the entire thick-mask DNF. Then, a fast high-NA EUV lithography imaging model with pupil obstruction is established, where the above mentioned thick-mask model is implanted.

Based on the fast high-NA EUV lithography imaging model, a gradient-based mask optimization (MO) algorithm is developed. Based on the low-pass filtering property of the imaging system and the convolution feature of the thick-mask model, the gradient of aerial image with respect to the mask pattern can be calculated analytically. Using the GPU device to implement the convolution operations, the MO algorithm can be accelerated about 10 times. Meanwhile, a compressive sensing (CS) algorithm is applied to construct the optimal source pattern with high imaging performance. Combining the source optimization (SO) and MO algorithms, the SMO method for high-NA EUV lithography is developed. Simulations show that the proposed SMO method can significantly improve the lithography image

fidelity by reducing about 70% patterning error. Meanwhile, the proposed method also shows high computational efficiency, which is critical for its further applications.

Imaging model for high-NA EUV lithography

This section describes the imaging model of high-NA EUV lithography system. First, the anamorphic magnification and central pupil obstruction of the projection system are discussed. Then, a fast learning-based thick-mask model is introduced. Combining all of the above-mentioned effects, the Abbe's imaging model of high-NA EUV lithography system is constructed. The proposed model is compared with a commercial software to verify its accuracy.

Figure 2(a) illustrates the transfer process of a layout pattern from the reflective mask to the wafer in the high-NA EUV lithography tool. First, the mask pattern should be modified according to the magnification factors. On the mask stage, the incidence EUV light is diffracted by the mask, and then generates the DNF, which further propagates through the projection system. Then, the aerial image is formed on the wafer. Finally, the resist is exposed by the aerial image on the wafer plane, where the layout contour is obtained after the development of resist.

Projection system with anamorphic magnification and pupil central obstruction

The high-NA EUV lithography tool adopts the projection system with anamorphic magnification and pupil central obstruction. The anamorphic projection system is used to separate the incoming and outgoing light paths[2,15,16]. The magnification is ×8 in y-direction, and ×4 in x-direction. Meanwhile, the workflow of the proposed imaging model is shown in Fig. 2(b), where the effect of anamorphic magnification is involved in the calculation of mask DNF.

Another feature of the high-NA EUV lithography system is the drilled optical design on the second-to-last mirror in the projection system, as illustrated in Fig. 1(c). The drilled optics can be represented as the pupil central obstruction, and the partial coherence factor (σ) of the obstruction on the pupil plane is 0.21[15]. The obstruction may lead to the loss of some frequency components, subsequently affects the lithography imaging quality[17]. Figure 3(a) shows the source plane of high-NA EUV lithography system, where the green cross at the spatial coordinate (0, 0) denotes the central source point, and the yellow cross at the spatial coordinate (−0.3, 0) denotes an adjacent source point. Figure 3(b) sketches the imaging processes under these two source points, respectively. On the left of Fig. 3(b), the red rings represent the pupil areas with central obstructions. In Fig. 3(b), the upper row shows the imaging under the central source point. For the "L-shape" pattern, a significant loss of frequency components occurs due to the central obstruction, resulting in an aerial image with poor fidelity. On the other hands, the imaging process of the other source point is shown in the lower row, where more frequency components are captured by the pupil, leading to an aerial image with superior quality. In a word, the pupil central

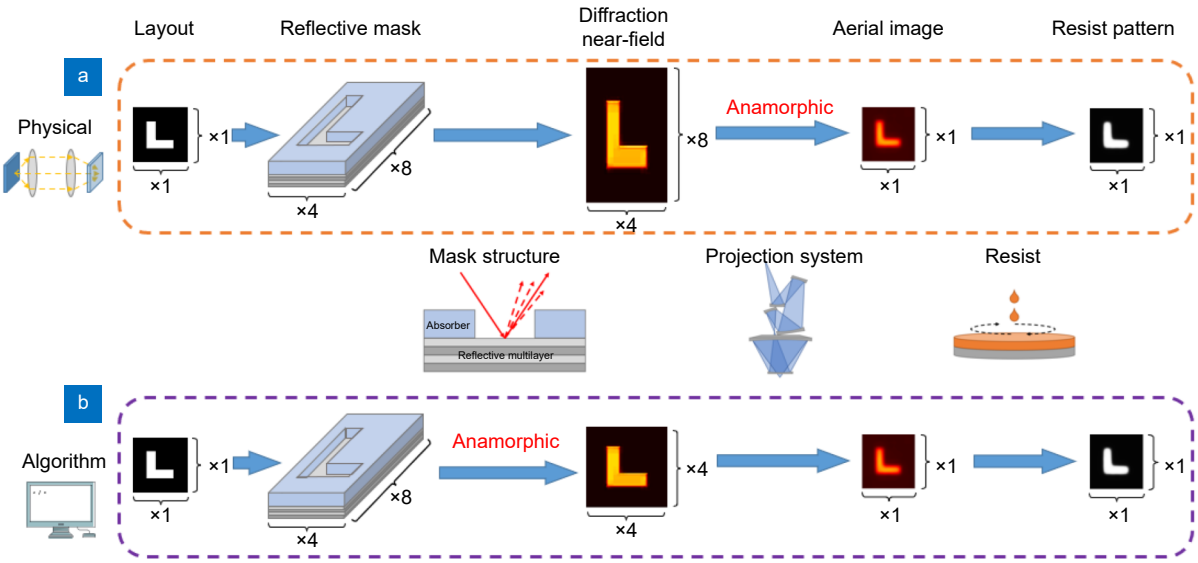

Fig. 2 | The flows of (**a**) the lithography process, and (**b**) the proposed imaging model.

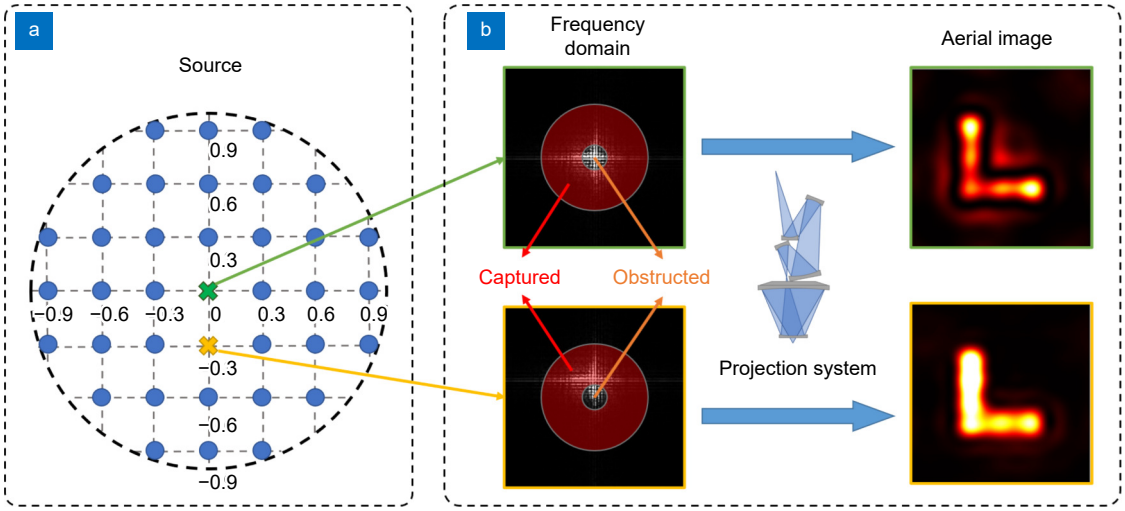

Fig. 3 | The illustrations of (**a**) the source plane, and (**b**) the impacts of central obstruction in the projection system.

obstruction degrades the imaging quality of the source points located at the central area, which further impacts the optimized source pattern.

Modelling of mask 3D effect

The mask 3D effect is a prominent effect that impacts the DNF distribution, and further affects the imaging in all EUV lithography tools[5–7]. The thick-mask DNF can be calculated with rigorous electromagnetic field (EMF) simulators[20,21]. However, those methods are computationally intensive, which is unacceptable for the SMO method. Therefore, to efficiently simulate the DNF with mask 3D effect, a decomposed-learning thick-mask model is applied in this work[7].

In general, the thick-mask model assumes that the mask structure is a shift-invariant system within a localized area, whose input is the mask pattern, while the output is the corresponding DNF. Therefore, the local DNF can be calculated as the convolution between the mask segment and a filter:

$$\boldsymbol{E}_{3\mathrm{D}} = \boldsymbol{C}_{3\mathrm{D}} \otimes \boldsymbol{M}, \tag{1}$$

where $\boldsymbol{M}$ denotes the binary mask segment, $\boldsymbol{C}_{3\mathrm{D}}$ is the convolution filter, $\otimes$ is the convolution symbol, and $\boldsymbol{E}_{3\mathrm{D}}$ is the calculated DNF of the mask segment. Based on the pre-established DNF database, the convolution filter of each feature and rotation can be inversely calculated.

Figure 4 depicts the process to calculate the DNF of a given thick mask pattern. Figure 4(a) displays an "L-shape" mask pattern as an instance. The mask pattern is first decomposed into segments according to its geometric feature (i.e. convex, concave, and edge), as shown in Fig. 4(b). Subsequently, as illustrated in Fig. 4(c), all of the mask segments are convoluted with their corresponding filters to calculate local DNFs. Finally, all of the local DNFs are composed together based on the weighted stitching algorithm in ref.[18,19], and the global

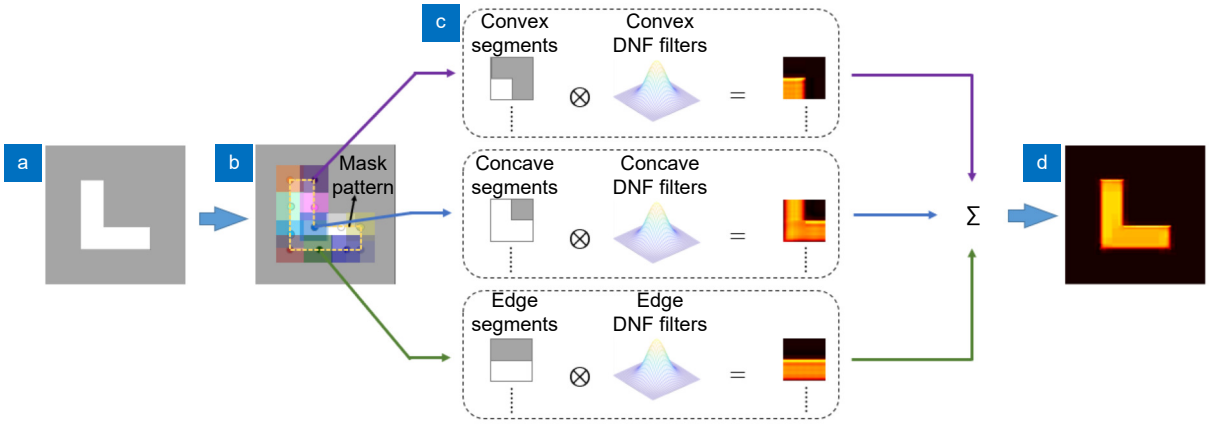

Fig. 4 | The flow of the thick-mask model. (**a**) The L-shape mask pattern. (**b**) The mask decomposition. (**c**) The DNF segments calculated based on convolution kernels. (**d**) The final combined DNF for the entire mask pattern.

thick-mask DNF is obtained, which is shown in Fig. 4(d). The global DNF can be expressed as:

$$\boldsymbol{E}_{3\mathrm{D}} = \sum_{l=1}^{4} \boldsymbol{C}_{\mathrm{edge},l} \otimes \boldsymbol{M}_{\mathrm{edge},l} + \sum_{l=1}^{4} \boldsymbol{C}_{\mathrm{conv},l} \otimes \boldsymbol{M}_{\mathrm{conv},l} + \sum_{l=1}^{4} \boldsymbol{C}_{\mathrm{conc},l} \otimes \boldsymbol{M}_{\mathrm{conc},l}, \quad (2)$$

where the subscript l denotes the rotation in 0°, 90°, 180°, or 270°; the subscript edge, conv, conc denote the edge, convex corner, and concave corner, respectively.

The thick-mask model mentioned above can simulate the EUV DNF with mask 3D effect accurately and efficiently. More importantly, the convolution-based thick-mask model can be integrated into the gradient-based MO algorithm intrinsically.

Abbe's imaging model

Abbe's imaging model is widely used to calculate the aerial image of lithography system[1,3,4], which can be expressed as:

$$\boldsymbol{I} = \frac{1}{\boldsymbol{J}_{\mathrm{sum}}} \sum_{x_\mathrm{s}} \sum_{y_\mathrm{s}} \left(\boldsymbol{J}(x_\mathrm{s}, y_\mathrm{s}) \left| \boldsymbol{H}^{x_\mathrm{s} y_\mathrm{s}} \otimes \left(\boldsymbol{B}^{x_\mathrm{s} y_\mathrm{s}} \odot \boldsymbol{E}_{3\mathrm{D}}^{x_\mathrm{s} y_\mathrm{s}}\right)\right|^2\right), \quad (3)$$

where $\boldsymbol{E}_{3\mathrm{D}}^{x_\mathrm{s} y_\mathrm{s}}$ denotes the mask DNF generated by the source point $(x_\mathrm{s}, y_\mathrm{s})$, which can be calculated using the above-mentioned thick-mask model. The scaler matrix $\boldsymbol{B}^{x_\mathrm{s}, y_\mathrm{s}}$ is the mask diffraction matrix, and $\odot$ denotes the element-wise product. $\boldsymbol{H}^{x_\mathrm{s}, y_\mathrm{s}}$ is the equivalent filter of the projection system under the specific source point, where the center obstruction of the high-NA EUV lithography is taken into account. $\boldsymbol{J}(x_\mathrm{s}, y_\mathrm{s})$ stands for the source point intensity, and $\boldsymbol{J}_{\mathrm{sum}}$ is a normalized factor.

A sigmoid function is further used to approximate the threshold effect of resist, so that the gradient of cost function exists during the optimization:

$$\mathrm{sig}(x) = \frac{1}{1 + \exp[-a(x - t_\mathrm{r})]}, \quad (4)$$

where t_r is the process threshold, and a is a coefficient that dictates the steepness of the sigmoid function. In this work, the threshold t_r is set as 0.3, and the coefficient a in the sigmoid function is set as 20.

In order to validate the accuracy of the proposed imaging model, the aerial image results calculated by the proposed model (left) and a commercial software (right) are compared in Fig. 5(a). The aerial images of mask patterns with 13 nm CD and 9 nm CD generated by a circular illumination (initial state in Section *Results of the SMO method*) are illustrated from top to bottom. Figure 5(b) illustrates the cross sections of the aerial images along the red line for the two mask patterns. The RMS errors of aerial images with 13 nm and 9 nm CD are 0.011 and 0.014 respectively, whose detailed definition can be found in ref.[7]. It is observed that the proposed model achieves commendable computational accuracy compared to the commercial software. On the other hand, the RMS error increases to 0.041 for curvilinear mask with 13 nm CD. The error is mainly caused by the thick mask model, and the accuracy of the imaging model is still acceptable.

The SMO method for high-NA EUV lithography

In this section, the proposed SMO method for high-NA EUV lithography is introduced in detail. The gradient-based MO algorithm and the CS-based SO algorithm are discussed respectively. The whole SMO workflow is constructed by combining the MO and SO algorithms.

Gradient-based MO algorithm

The purpose of the MO algorithm is to find the optimal mask pattern, which can improve the similarity between the target pattern and the resist pattern. Therefore, in this study, the cost function F is set as the square of the L2-norm of the distance between the final resist pattern $\boldsymbol{R}$ and the target pattern $\boldsymbol{Z}$:

$$F = \|\boldsymbol{Z} - \boldsymbol{R}\|_2^2, \quad (5)$$

where the cost function F can be used to assess the imaging quality.

Let $\boldsymbol{M} \in \Re^{N \times N}$ denotes the optimal mask pattern such that the cost function in Eq. (5) is minimized. The MO problem can be thus formulated as:

$$\boldsymbol{M} = \underset{\mathbf{M} \in \Re^{N \times N}}{\operatorname{argmin}} F. \quad (6)$$

In this work, the binary EUV mask is studied, where the reflective area is represented as 1, and absorbed aera is 0. In order to reduce the bound-constrained optimization problem in Eq. (6) to an unconstrained one, the parametric transformation in ref.[22] is adopted in this work:

$$\boldsymbol{M} = f(\Omega) = 0.5(1 + \cos\Omega), \quad (7)$$

where the Ω is the transformation parameter.

Owing to the shift-invariant nature of the thick-mask model and the imaging model, the calculation of aerial image gradient is fundamentally based on convolution.

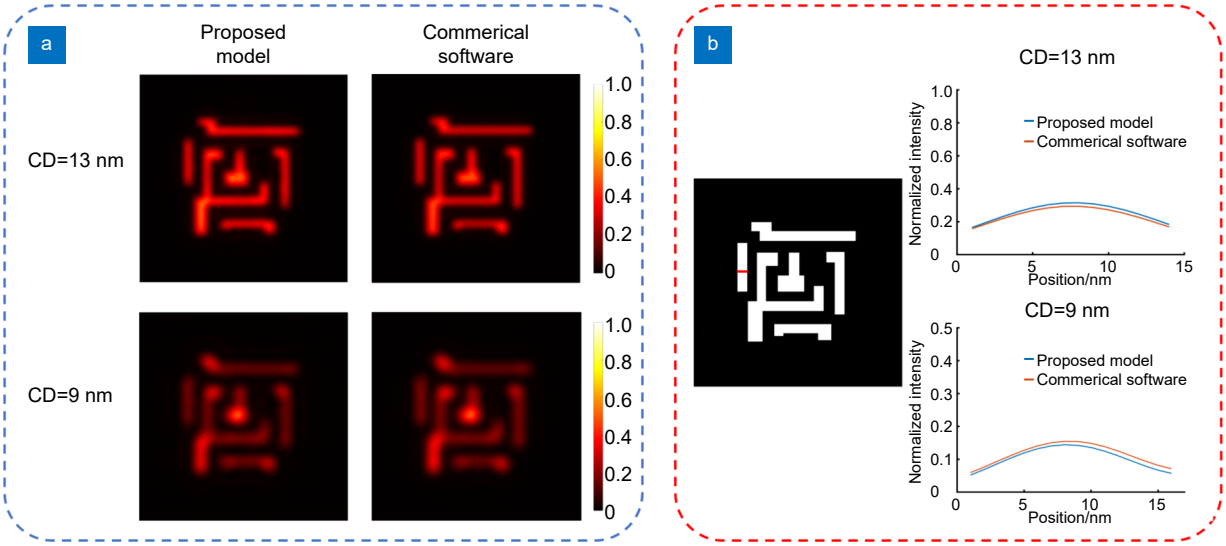

Fig. 5 | The comparison of the proposed imaging model and a commercial software. (**a**) The aerial images of the mask patterns with 13 nm CD and 9 nm CD that are calculated by the proposed model (left) and commercial software (right), and (**b**) the cross sections of the normalized aerial images along the red line.

The steepest descent (SD) algorithm is used to optimize the mask pattern, and the gradient $\nabla F(\Omega)$ can be calculated as follow:

$$\begin{aligned}\nabla F(\Omega) =& \frac{\partial F}{\partial \boldsymbol{R}} \cdot \frac{\partial \boldsymbol{R}}{\partial \boldsymbol{I}} \cdot \frac{\partial \boldsymbol{I}}{\boldsymbol{M}} \cdot \frac{\partial \boldsymbol{M}}{\partial \Omega} = \frac{a}{J_{\text{sum}}} f'(\Omega) \\ & \odot \sum_{x_{\text{s}}} \sum_{y_{\text{s}}} \boldsymbol{J}(x_{\text{s}}, y_{\text{s}}) \times \sum_{f} \sum_{l} \text{Re}\left\{ (\boldsymbol{B}^{x_{\text{s}} y_{\text{s}}})^{*} \right. \\ & \left. \odot \left[(\boldsymbol{H}^{x_{\text{s}} y_{\text{s}}} \otimes \boldsymbol{C}_{l,f}^{x_{\text{s}} y_{\text{s}}})^{*T} \otimes (\boldsymbol{E}_{\text{wafer},l,f}^{x_{\text{s}} y_{\text{s}}} \odot \Lambda_{l,f}) \right] \right\},\end{aligned} \tag{8}$$

where the $\Lambda_{l,f} = (\boldsymbol{Z}_{l,f} - \boldsymbol{R}_{l,f}) \odot \boldsymbol{R}_{l,f} \odot (1 - \boldsymbol{R}_{l,f})$, and the $\boldsymbol{E}_{\text{wafer},l,f}^{x_{\text{s}} y_{\text{s}}}$ denotes the electric field generated by the $(x_{\text{s}}, y_{\text{s}})$ source point on the wafer plane, which can be calculated as: $\boldsymbol{E}_{\text{wafer},l,f}^{x_{\text{s}} y_{\text{s}}} = \boldsymbol{H}^{x_{\text{s}} y_{\text{s}}} \otimes (\boldsymbol{B}^{x_{\text{s}} y_{\text{s}}} \odot \boldsymbol{C}_{l,f}^{x_{\text{s}} y_{\text{s}}} \otimes \boldsymbol{M}_{l,f})$. Subscripts l and f denote the rotation and feature category of the pattern respectively.

Assuming the Ω^m is the optimized result after mth iteration, then at the $(m+1)$th iteration:

$$\Omega^{m+1} = \Omega^m - s_\Omega \nabla F(\Omega), \tag{9}$$

where the s_Ω is the step length. The SD algorithm is terminated when the iteration number m reaches the prescribed upper limit.

In general, the above optimization procedure leads to a grayscale mask. Therefore, the final binary mask $\boldsymbol{M}_{\text{b}}$ is the binary quantization of the $\boldsymbol{M}$:

$$\boldsymbol{M}_{\text{b}} = \Gamma(\boldsymbol{M} - t_m), \tag{10}$$

where the t_m =0.5 is the global threshold. $\Gamma(\cdot) = 1$ if the argument is larger than 0, while $\Gamma(\cdot) = 0$ otherwise.

It should be noticed that, in the gradient calculation, the filter kernels of mask 3D model and aerial image model are convoluted together. Thus, those filter kernels under different source points can be pre-calculated to improve the computational efficiency. Additionally, the gradient calculation is also the most time-consuming step in the MO algorithm. By migrating the convolution operation to GPU devices, the speed of gradient calculation can be impressively improved, achieving approximately tenfold acceleration.

CS based SO algorithm

In this work, the CS algorithm is applied to solve for the optimal source pattern with high imaging performance[23,24]. Firstly, the aerial image model is transferred into the form of matrix multiplication:

$$\boldsymbol{I} = \boldsymbol{I}_{\text{CC}} \boldsymbol{J}, \tag{11}$$

where $\boldsymbol{I} \in \Re^{N^2 \times 1}$ and $\boldsymbol{J} \in \Re^{N_{\text{S}}{}^2 \times 1}$ denote the vectorized representations of the aerial image and source pattern, respectively. The notation $\boldsymbol{I}_{\text{CC}} \in \Re^{N^2 \times N_{\text{S}}{}^2}$ represents the illumination cross coefficient (ICC) matrix indicating the mapping form the source pattern to the aerial image, which can be calculated by the above-mentioned imaging model.

Suppose the vectorized source pattern $\boldsymbol{J}$ can be sparsely represented in a certain basis $\boldsymbol{\Psi} \in \Re^{N_{\text{S}}{}^2 \times N_{\text{A}}}$ $(N_{\text{A}} \geqslant N_{\text{S}}{}^2)$, thus $\boldsymbol{J} = \boldsymbol{\Psi\Theta}$ where $\boldsymbol{\Theta} \in \Re^{N_{\text{A}} \times 1}$ is the sparse coefficient vector. Then, the SO problem can be refor-

mulated as

$$\begin{aligned}\widehat{\boldsymbol{\Theta}} &= \underset{\boldsymbol{\Theta}}{\operatorname{argmin}} \|\boldsymbol{\Theta}\|_1 s.t.\ \boldsymbol{\Phi Z} = \boldsymbol{\Phi I} \\ &= \boldsymbol{\Phi I}_{\mathrm{CC}} \boldsymbol{J} = \boldsymbol{\Phi I}_{\mathrm{CC}} \boldsymbol{\Psi \Theta}\end{aligned} \tag{12}$$

where $\boldsymbol{\Phi} \in \Re^{L\times M}$ (L<M) is a projection matrix to reduce the dimensionality of the linear constraint equations, and $\boldsymbol{Z}$ denotes the vectorized target pattern. In this work, the linearized Bergman algorithm is adopted to solve the problem in Eq. (12) due to its high efficiency[23,25]. After obtaining the optimized coefficient vector $\widehat{\boldsymbol{\Theta}}$, the optimized source can be calculated by:

$$\widehat{\boldsymbol{J}} = \boldsymbol{\Psi}\widehat{\boldsymbol{\Theta}}\,, \tag{13}$$

from which the optimized source pattern can be further restored.

Flow of the proposed SMO method

The flow chart in Figure 6(b) illustrates the primary procedure of the SMO method. The thick mask DNF filters and the imaging filters, as described in Section 2, are precalculated, so that filters can be reused, and the efficiency of the algorithm can be improved. The algorithm then initializes, where the initial mask pattern is designated as the input layout, and the initial source pattern is defined as a full pupil illumination with normalized dose.

The source is optimized via the CS based SO algorithm afterwards, whose procedural outline is depicted in Fig. 6(a). The mask pattern is loaded, and the corresponding ICC matrix is calculated using the high-NA EUV lithography imaging model. Next, the critical region of the pattern is sampled to reduce the dimensionality of the SO problem. The linearized Bergman algorithm is then commenced, iterating until it reaches a predetermined iteration limit. Finally, the sparse coefficient is obtained, and the optimized source pattern is further reconstructed from it.

Following the SO algorithm, the gradient-based MO algorithm starts, and its flow chart is shown in Fig. 6(c). The optimized source pattern is initially loaded. Then, the gradient of cost function is calculated based on the Eq. (8), and the mask pattern is updated following the direction of steepest gradient. The iteration terminates as it reaches the prescribed limit. Finally, the mask pattern is optimized.

The proposed SMO method is developed by combining the SO and MO algorithm. Consecutive rounds of both algorithms iteratively proceed, aiming to minimize the cost function. Finally, the optimized mask and source pattern are obtained.

Results and discussion

Results of the SMO method

In this section, the results of the proposed SMO method

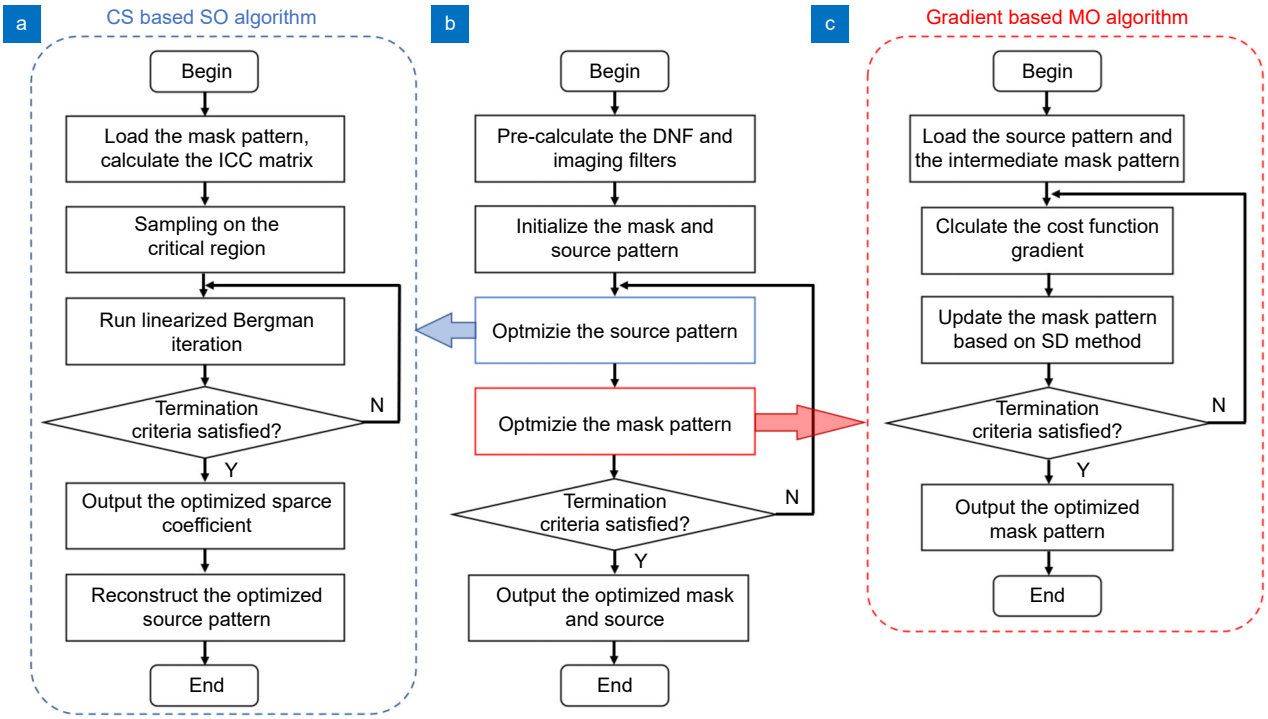

Fig. 6 | The flowcharts of (**a**) the SO algorithm, (**b**) the main SMO method, and (**c**) the MO algorithm.

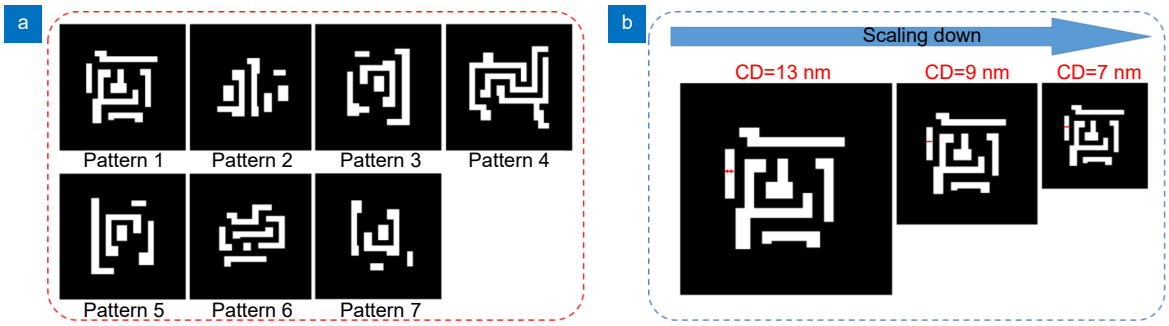

Fig. 7 | The Illustration of (**a**) the seven testing layout patterns, and (**b**) scaling down of a mask pattern.

are provided and discussed. All of the simulation codes are implemented by MATLAB, and the computations are carried out on a computer with Intel(R) Core(TM) i7-10870H CPU, 2.20 GHz, 32.0 GB of RAM, and NVIDIA GeForce RTX 3070 Laptop GPU. The optimization of the mask patterns with different CDs are studied. The algorithms are tested on seven layout patterns in this work. Figure 7(a) shows the seven testing layouts, and Fig. 7(b) illustrates the sketch of a mask pattern with different CDs. The resolution of the layouts is 1 nm, and lateral dimensions of layouts in 13 nm, 9 nm, 7 nm CDs are 300 nm, 200 nm, and 150 nm, respectively. Notices that, all dimensions are in the wafer scale. Meanwhile, the sigmoid function in Eq. 4 is applied for the resist model. Due to the length limit of this paper, only results of pattern #1 and pattern #2 are illustrated in detailed, and the results for all of the seven layouts are listed in tables.

Figures 8, 9, and 10 present the optimization results for two patterns with various CDs. Results of pattern #1 are shown on the left, while results of pattern #2 are shown on the right. For each simulation, the initial and optimized mask patterns, source patterns, and resist images are displayed.

In Fig. 8(a), the optimized resist image shows tremendous improvement in imaging quality compared to the initial resist image. The value of loss function de-

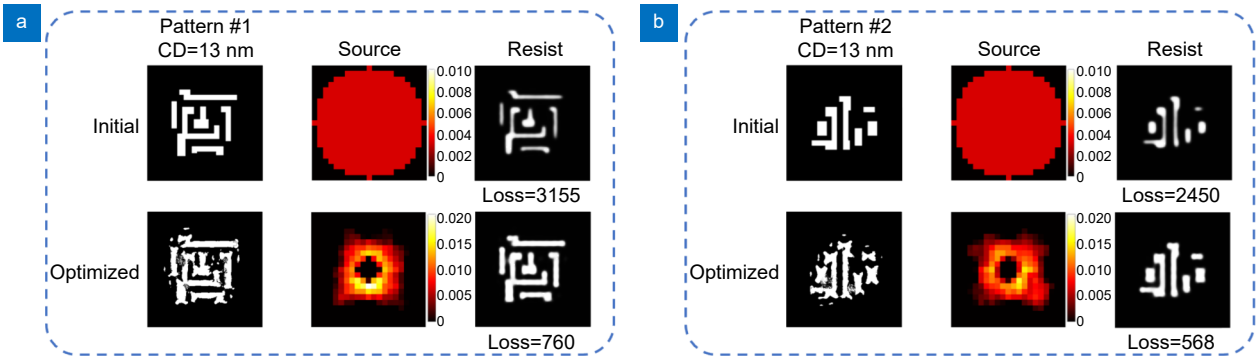

Fig. 8 | The optimization results obtained by the proposed SMO method. (**a**) and (**b**) show the results of pattern #1 and pattern #2 with 13 nm CD.

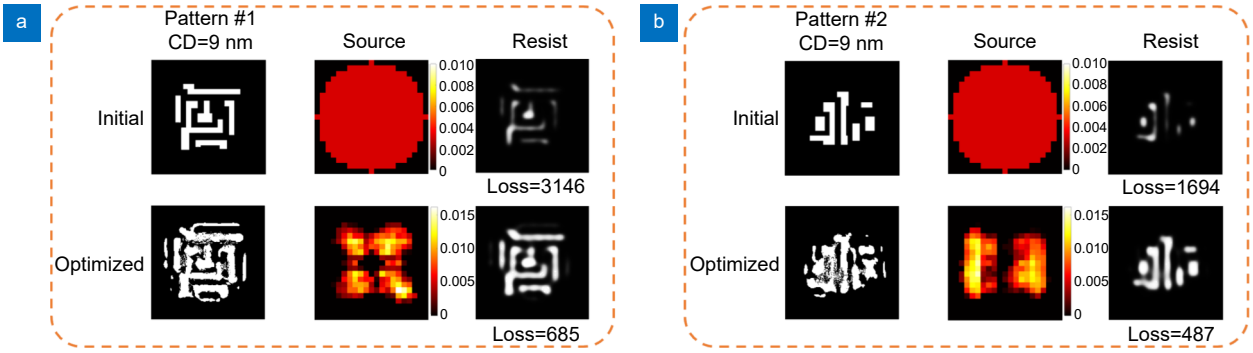

Fig. 9 | The optimization results obtained by the proposed SMO method. (**a**) and (**b**) show the results of pattern #1 and pattern #2 with 9 nm CD.

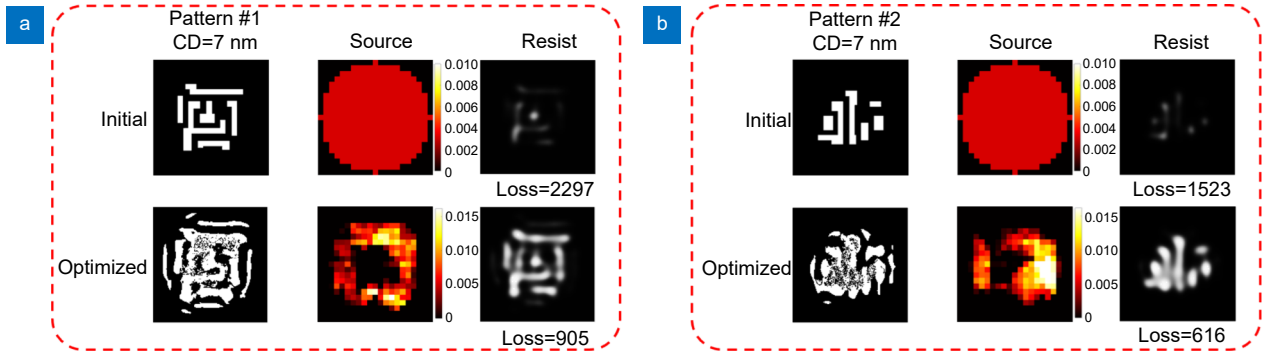

Fig. 10 | The optimization results obtained by the proposed SMO method. (**a**) and (**b**) show the results of pattern #1 and pattern #2 with 7 nm CD.

creases from 3155 to 760. Meanwhile, the corresponding optimization results of pattern #2 with 13 nm CD are shown in Fig. 8(b), noting a reduction of loss function from 2450 to 568. Table 1 lists the initial losses, post-optimization losses, and computation times for different testing patterns with 13 nm CD. The proposed SMO method can reduce the loss by 73% in average, and takes about 160 s for calculation.

Figure 9(a) shows a marked reduction of loss function value from 3146 to 685, and Fig. 9(b) shows a decline of the loss from 1694 to 487. Table 2 lists the initial losses, post-optimization losses, and computation times for different testing patterns with 9 nm CD. The proposed SMO method can reduce the loss by 71% in average, and takes 155 s for calculation.

Table 1 | Initial losses, optimized losses, and runtimes of the SMO method based on different testing layouts with 13 nm CD.

Pattern No.	Initial loss	Optimized loss	Calculation time/s
1	3155	760	168
2	2450	568	159
3	2680	791	159
4	3202	974	161
5	2558	623	153
6	2630	638	161
7	2104	695	152

Table 2 | Initial losses, optimized losses, and runtimes of the SMO method based on different testing layouts with 9 nm CD.

Pattern No.	Initial loss	Optimized loss	Calculation time/s
1	3146	685	155
2	1694	487	162
3	2211	668	150
4	2968	1085	161
5	2004	659	141
6	2486	772	167
7	1687	461	153

Figure 10(a) and 10(b) show the optimization results with 7 nm CD. It is observed that the initial source and mask can hardly print any pattern on the resist. On the other hand, the loss function for pattern #1 decreases from 2297 to 905 after the optimization, and the loss function for pattern #2 with 7 nm decreases from 1523 to 616 after the optimization. Despite of the improvement of imaging fidelity, the optimized patterns are still sub-optimal for the IC fabrication. These results suggest that high-NA EUV lithography with single patterning is hardly to manufacture arbitrary patterns with 7 nm CD. Instead, high-NA EUV lithography with multiple patterning or other advanced patterning techniques should by applied for the fabrication of such small features.

Table 3 summarizes the initial losses, post-optimization losses, and computation times for different testing patterns with 7 nm CD. The proposed SMO method can reduce the loss by 63% in average, and takes 167 s for calculation.

It is noted that all of the computational times mentioned above are performed on GPU device. As a comparison, the SMO method will take about 1300 s to run on the CPU device. Therefore, using GPU device can accelerate the SMO method by tenfold, which is valuable for its applications.

In addition, for all of the layout patterns with differ-

Table 3 | Initial losses, optimized losses, and runtimes of the SMO method based on different testing layouts with 7 nm CD.

Pattern No.	Initial loss	Optimized loss	Calculation time/s
1	2297	905	163
2	1523	616	162
3	1791	568	165
4	2819	1106	176
5	1739	565	168
6	1875	823	187
7	1433	524	154

ent CDs, the source points located in the center pupil area yield poor-fidelity aerial images. Therefore, the SO algorithm inherently designates lower intensities to the central source area. This observation is attributed to the central pupil obstruction of the high-NA EUV projection system, which has been discussed in Section *Projection system with anamorphic magnification and pupil central obstruction*.

Results of the MRC process

The mask rule check (MRC) is an important process to improve the manufacturability of the designed layout. Meanwhile, the constrain of mask pattern complexity will also degrade the imaging inevitably. In this section, we proposed an MRC process to simplify the optimized mask pattern after the SMO.

Firstly, the mask pattern is simplified preliminarily by reducing Harr-wavelet complexity penalty[26]. Then, the MRC process starts, including down-sampling the mask, eliminating small isolated holes and protrusions, converting all irregular sub-resolution assist features (SRAFs) into rectangles. Notice that, the anamorphic magnification of high-NA EUV system should be considered in the MRC process. In this work, we assume the beam size of a multi-beam mask writer is 16 nm[27], so that it should be converted to 4 nm in x-direction and 2 nm in y-direction in the wafer scale.

Figure 11 shows the results of the MRC process. Figure 11(a) shows the target pattern and an optimized source pattern from top to the bottom. The optimized mask pattern and its corresponding resist pattern are displayed in Fig. 11(b), where the imaging loss is 757. On the other hands, the mask pattern after MRC and its resist pattern are shown in Fig. 11(c), where the imaging loss increase to 926. It is shown that, the MRC process can significantly reduce the complexity of the mask pattern, and its negative impact to the imaging is acceptable.

Conclusion

This work proposed an SMO method for high-NA EUV lithography system. Firstly, the imaging models for high-NA EUV lithography was established, where the anamorphic magnification, pupil central obstruction and mask 3D effect were considered. The accuracy of the imaging model was verified based on the comparison to a commercial software. Then, the SMO method for high-NA EUV lithography system was developed by combining the CS-based SO algorithm and the gradient-based MO algorithm. An MRC process is further conducted to simplify the optimized mask pattern. Simulation results showed that the proposed SMO method can reduce the imaging loss by 70% on average for different testing layouts across various CDs. According to the imaging improvement and the high computational efficiency, the proposed SMO method is valuable to the EUV litho-

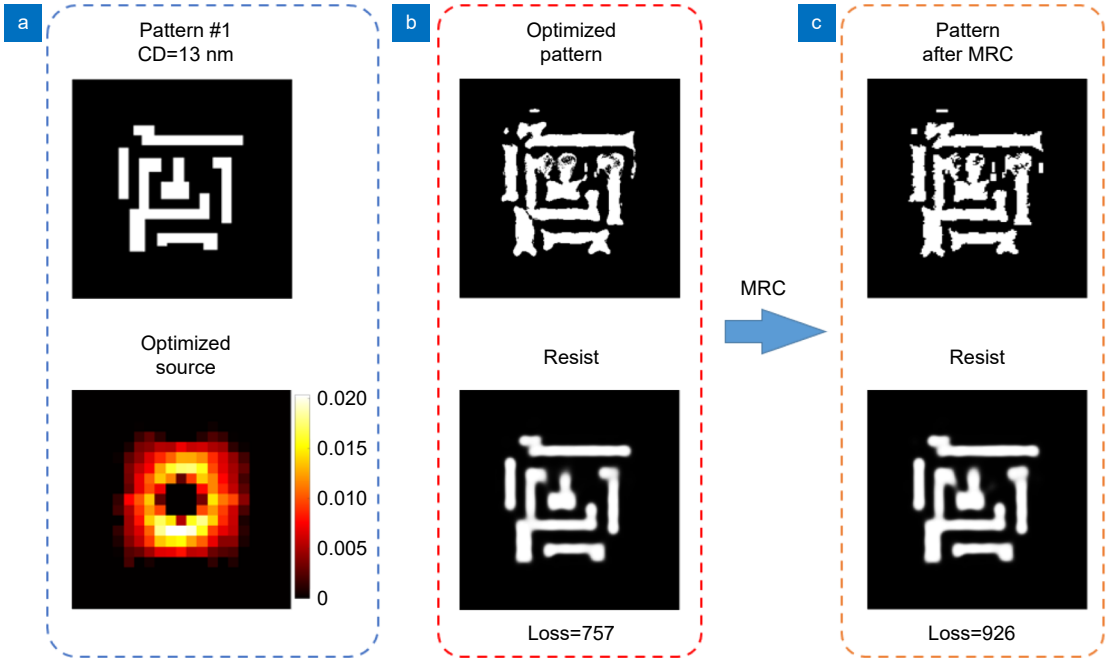

Fig. 11 | Results of the MRC. (**a**) The target mask and the illumination condition. (**b**) The optimized mask pattern and its resist pattern. (**c**) The mask after MRC and its resist pattern.

graphy process at advanced IC technology nodes.

References

1. Erdmann A. *Optical and EUV Lithography*: *A Modeling Perspective* (SPIE Press, Bellingham, 2021).
2. Bakshi V. *EUV Lithography* (SPIE Press, Bellingham, 2009).
3. Mack C. *Fundamental Principles of Optical Lithography*: *the Science of Microfabrication* (John Wiley & Sons, Chichester, 2007).
4. Ma X, Arce GR. *Computational Lithography* (John Wiley & Sons, Hoboken, 2010).
5. Lin JX, Dong LS, Fan TA et al. Fast aerial image model for EUV lithography using the adjoint fully convolutional network. *Opt Express* **30**, 11944–11958 (2022).
6. Liu P, Xie XB, Liu W et al. Fast 3D thick mask model for full-chip EUVL simulations. *Proc SPIE* **8679**, 86790W (2013).
7. Li ZQ, Jing XY, Dong LS et al. Fast diffraction model of an EUV mask based on asymmetric patch data fitting. *Appl Opt* **62**, 6561–6570 (2023).
8. Shiraishi M, Oshino T, Murakami K et al. Flare modeling and calculation on EUV optics. *Proc SPIE* **7636**, 763629 (2010).
9. Rosenbluth AE, Bukofsky SJ, Fonseca CA et al. Optimum mask and source patterns to print a given shape. *J Micro/Nanolithogr MEMS MOEMS* **1**, 13–30 (2002).
10. Pan YH, Ma X, Zhang SE et al. Efficient informatics-based source and mask optimization for optical lithography. *Appl Opt* **60**, 8307–8315 (2021).
11. Ma X, Dong LS, Han CY et al. Gradient-based joint source polarization mask optimization for optical lithography. *J Micro/Nanolithogr MEMS MOEMS* **14**, 023504 (2015).
12. Ma X, Wang ZQ, Chen XB et al. Gradient-based source mask optimization for extreme ultraviolet lithography. *IEEE Trans Comput Imaging* **5**, 120–135 (2019).
13. Zou LL, Sun YY, Wei PZ et al. Exposure latitude aware source and mask optimization for extreme ultraviolet lithography. *Appl Opt* **60**, 9404–9410 (2021).
14. Zhang ZN, Li SK, Wang XZ et al. Source mask optimization for extreme-ultraviolet lithography based on thick mask model and social learning particle swarm optimization algorithm. *Opt Express* **29**, 5448–5465 (2021).
15. Gao WM, Zhu BE, Chiou TB et al. Computational lithographic study of 0.55 NA EUV single patterning for metal layers for the 2nm logic node and beyond. *Proc SPIE* **12052**, 120520G (2022).
16. van Schoot J, van Setten E, Rispens G et al. High-numerical aperture extreme ultraviolet scanner for 8-nm lithography and beyond. *J Micro/Nanolithogr MEMS MOEMS* **16**, 041010 (2017).
17. Gao WM, Chen CK, Zimmermann J. Computational evaluation of critical logical metal layers of pitch 20-24nm and the aberration sensitivity in high NA EUV single patterning. *Proc SPIE* **12495**, 1249509 (2023).
18. Li ZQ, Dong LS, Ma X et al. Decomposition-learning-based thick-mask model for partially coherent lithography system. *Opt Express* **31**, 20321–20337 (2023).
19. Li ZQ, Dong LS, Jing XY et al. High-precision lithography thick-mask model based on a decomposition machine learning method. *Opt Express* **30**, 17680–17697 (2022).
20. Azpiroz JT, Burr GW, Rosenbluth AE et al. Massively-parallel FDTD simulations to address mask electromagnetic effects in hyper–NA immersion lithography. *Proc SPIE* **6924**, 69240Y (2008).
21. Lee SG, Lee KI, Lee JU et al. More stable algorithm for rigorous coupled wave analysis applied to topography simulation in optical lithography and its numerical implementation. *Proc SPIE* **2726**, 288–298 (1996).
22. Ma X, Han CY, Li YQ et al. Hybrid source mask optimization for robust immersion lithography. *Appl Opt* **52**, 4200–4211 (2013).
23. Ma X, Shi DX, Wang ZQ et al. Lithographic source optimization based on adaptive projection compressive sensing. *Opt Express* **25**, 7131–7149 (2017).
24. Lin JX, Dong LS, Fan TA et al. Learning-based compressive sensing method for EUV lithographic source optimization. *Opt Express* **27**, 22563–22581 (2019).
25. Cai JF, Osher S, Shen ZW. Linearized Bregman iterations for compressed sensing. *Math Comput* **78**, 1515–1536 (2009).
26. Poonawala A, Milanfar P. Mask design for optical microlithography—an inverse imaging problem. *IEEE Trans Image Process* **16**, 774–788 (2007).
27. Yasuda J, Nomura H, Matsumoto H et al. Recent progress and future of electron multi-beam mask writer. *Jpn J Appl Phys* **62**, SG0803 (2023).

Acknowledgements

This work was financially supported by National Natural Science Foundation of China (No. 62274181，62204257 and 62374016), Chinese Ministry of Science and Technology (No. 2019YFB2205005), Guangdong Province Research and Development Program in Key Fields (No. 2021B0101280002). We acknowledge the support from Youth Innovation Promotion Association Chinese Academy of Sciences (No. 2021115), Beijing Institute of Electronics, Beijing Association for Science and Technology as well. And the authors would like to thank the support from University of Chinese Academy of Sciences (No. 118900M032) and China Fundamental Research Funds for the Central Universities (No. E2ET3801).

Competing interests

The authors declare no competing financial interests.

Scan for Article PDF